Solution of the Unsteady Euler Equations in Three Dimensions Using a Fully Unfactored Method

K.Badcock, M. Woodgate, F. Cantariti, and B. Richards
Aerospace Engineering Report 9909

Aerospace Engineering Department, University of Glasgow, Glasgow G12 8QQ, U.K.

Abstract

An unfactored implicit time-marching method for the solution of the unsteady three dimensional Euler equations is presented. For robustness the convective terms are discretised using an upwind TVD scheme while the unsteady equations are discretised using the implicit pseudo time approach. The pseudo steady state problem is solved using an unfactored implicit method. The linear system arising from each pseudo time step is solved using a Krylov subspace method with preconditioning based on a block incomplete lower-upper (BILU(0)) factorisation. The method in parallel yields high efficiency. Results are shown for unsteady forced pitched WEAG-TA15, LANN and F5 wings to illustrate the efficient performance of the method and the fast calculation times achieved on a PC.

1 Introduction

There has been an upsurge of interest in recent years in unsteady aerodynamics. Applications associated with aeroelasticity, dynamic stall, cavity flows, buffet and manouevering all lead naturally to unsteady flows. Advances in numerical methods and computers, coupled with the problem of data collection for unsteady experiments, has lead to increased interest in simulation for these problems. However, the calculation of three dimensional unsteady flows is a formidable computational problem.

There are a number of issues which are important for unsteady flow simulation. These include grid adaption and treatment for moving geometries. The calculations presented herein are on multiblock structured grids which are restrictive from the point of view of adaption. Previous work ([15]) showed how transfinite interpolation of displacements could be used to modify meshes when boundaries are in motion.

The crucial number issue is that the time step should be chosen solely for time accuracy. This is important because the calculations should be no more expensive than is required. Implicit methods are attractive from this point of view because they do not suffer from the stability restrictions of explicit methods. However, some form of approximation was often used for conventional implicit methods to reduce the storage requirements for large matrices, and to make solving the resulting large linear systems cheaper. Examples include the ADI method [8], the LU factorisation method [18] and the FUN method [12]. These approximations have the effect of limiting the usuable time step.

The pseudo time approach was introduced in [1]. In this formulation the calculation of the updated flow solution proceeds by solving for a steady state, which can be calculated in the same way as a normal flow steady state by using methods such a multigrid. This has proved very effective.

The current paper uses an unfactored solver to solve for the pseudo steady states within the pseudo time method. This method has proved effective for solving flow steady state problems in 3d [16] and steady [3] [7] and unsteady problems [15] [13] in two dimensions. The method is evaluated in the current paper, using flow over pitching LANN, F5 and a delta wing as the test cases.

2 Mathematical Model

The three-dimensional Euler equations can be written in non-dimensional conservative form and Cartesian coordinates as

$$\partial \mathbf{W}_t + \partial \mathbf{F}_x + \partial \mathbf{G}_y + \partial \mathbf{H}_z = 0 \qquad (1)$$

where $\mathbf{W} = (\rho, \rho u, \rho v, \rho w, \rho E)^T$ denotes the vector of conservative variables. The flux vectors $\mathbf{F}$, $\mathbf{G}$ and $\mathbf{H}$ are,

$$\mathbf{F} = \begin{pmatrix} \rho U \\ \rho u U + p \\ \rho v U \\ \rho w U \\ U(\rho E + p) + x_t p \end{pmatrix},$$

$$\mathbf{G} = \begin{pmatrix} \rho V \\ \rho u V \\ \rho v V + p \\ \rho w V \\ V(\rho E + p) + y_t p \end{pmatrix},$$

$$\mathbf{H} = \begin{pmatrix} \rho W \\ \rho u W + p \\ \rho v W \\ \rho w W + p \\ W(\rho E + p) + z_t p \end{pmatrix}.$$

In the above ρ, u, v, w, p and E denote the density, the three Cartesian components of the velocity, the pressure and the specific total energy respectively. The terms U, V and W are the contravariant velocities defined by

$$U = u - x_t, \qquad V = v - y_t, \qquad W = w - z_t$$

where x_t, y_t and z_t are the grid speeds in the coordinate directions.

3 The Unfactored Method

The Euler equations are discretised using a cell-centred finite volume method which converts the partial differential equations of (1) into a set of ordinary differential equations which can be written as

$$\frac{d}{dt}(V_{i,j,k}\mathbf{W}_{i,j,k}) = -\mathbf{R}_{i,j,k}(\mathbf{W}). \tag{2}$$

The convective terms are discretised using Osher's upwind scheme [19] for its robustness,accuracy and stability properties. MUSCL variable extrapolation is used to provide second-order accuracy with the Van Albada limiter to prevent spurious oscillations around shock waves. Boundary conditions are set by using ghost cells on the exterior of the computational domain. In the far field ghost values are set at the freestream conditions. At solid boundaries ghost values are extrapolated from the interior, ensuring that the normal component of the velocity on the solid wall is zero.

The present work extends the method introduced in [15] into three dimensions. The implicit dual-time approach follows that of Jameson [1]. Considering the semi discrete equation (2), this is discretised using a fully implicit method in time. Using a second-order backward difference in time this gives

$$\frac{3V^{n+1}_{i,j,k}\mathbf{W}^{n+1}_{i,j,k} - 4V^{n}_{i,j,k}\mathbf{W}^{n}_{i,j,k} + V^{n-1}_{i,j,k}\mathbf{W}^{n-1}_{i,j,k}}{2\Delta t} =$$

$$-\mathbf{R}_{i,j,k}(\mathbf{W}^{n+1}). \tag{3}$$

For ease of notation let us define a new residual $\mathbf{R}^\star$ by

$$\mathbf{R}^\star_{i,j,k}(\mathbf{W}^{n+1}) = \tag{4}$$

$$\frac{3V^{n+1}_{i,j,k}\mathbf{W}^{n+1}_{i,j,k} - 4V^{n}_{i,j,k}\mathbf{W}^{n}_{i,j,k} + V^{n-1}_{i,j,k}\mathbf{W}^{n-1}_{i,j,k}}{2\Delta t}$$

$$+\mathbf{R}_{i,j,k}(\mathbf{W}^{n+1}).$$

The problem of calculating the updated flow solution at time n+1 is now formulated as the steady state problem $\mathbf{R}^\star_{i,j,k}(\mathbf{W}^{n+1}) = 0$. A pseudo-time, $t^\star$, is introduced to write the problem of solving for the pseudo steady state as

$$\frac{d}{dt^\star}(V^{n+1}_{i,j,k}\mathbf{W}^{n+1}_{i,j,k}) = -\mathbf{R}^\star_{i,j,k}(\mathbf{W}^{n+1}). \tag{5}$$

The advantage of this approach is that the real time step can be chosen for time accuracy alone. If the pseudo steady state problem can be solved efficiently then the resulting method is efficient. This can be done using any time-marching technique, utilising any of the standard acceleration techniques, to obtain the pseudo steady state solution and hence the updated flow solution (3). In the current paper we use an unfactored implicit method to solve this problem.

The implicit time marching scheme for equation (5) in pseudo-time is given by

$$\frac{\mathbf{W}^{m+1}_{i,j,k} - \mathbf{W}^{m}_{i,j,k}}{\Delta t^\star} = -\frac{1}{V_{i,j,k}}\mathbf{R}^\star_{i,j,k}(\mathbf{W}^{m+1}) \tag{6}$$

where the superscript $m+1$ denotes the pseudo time level m+1. In order to solve equation (6) the term $\mathbf{R}^\star_{i,j,k}(\mathbf{W}^{m+1})$ is linearised with respect to the pseudo time:

$$\mathbf{R}^\star_{i,j,k}(\mathbf{W}^{m+1}) \approx \mathbf{R}^\star_{i,j,k}(\mathbf{W}^{m}) + \frac{\partial \mathbf{R}^\star_{i,j,k}}{\mathbf{W}_{i,j,k}}\Delta\mathbf{W}_{i,j,k} \tag{7}$$

where $\Delta\mathbf{W}_{i,j,k} = \mathbf{W}^{m+1}_{i,j,k} - \mathbf{W}^{m}_{i,j,k}$. Using this and equation (4) one implicit pseudo time step results in the linear system

$$\left[\left(\frac{V_{i,j,k}}{\Delta t^\star} + \frac{3V_{i,j,k}}{2\Delta t}\right)\mathbf{I} + \partial\mathbf{R}_{i,j,k}\mathbf{W}_{i,j,k}\right]\Delta\mathbf{W}_{i,j,k} = \tag{8}$$

$$-\mathbf{R}^\star_{i,j,k}(\mathbf{W}^{m}).$$

In the present work the left hand side of equation (8) is approximated with Jacobian matrices resulting from the first order spatial discretisation as in [7]. This nearly halves the number of terms in the matrix from 325 per cell to 175 which results in a substantial reduction in memory requirements as problems can easily have 10^6 cells. The right hand side of (8) is not changed so that at convergence high order spatial accuracy is maintained. A Krylov subspace algorithm is used to solve the linear system of equation and is preconditioned using a Block Incomplete Lower-Upper (BILU) factorisation which has the same sparsity pattern as the Jacobian matrix (BILU(0)). To aid parallel efficiency the BILU(0) factorisation is decoupled between blocks. The reduction in the effectiveness of the preconditioner as the number of block increases is small [14].

This method of solving for a steady state has proved efficient for calculating (real time) steady states. For example, for the transonic flow over the ONERA M6 wing the unfactored method has yielded fully converged results in less than one third of the time of a two factored method [12] [6]. The unfactored results were obtained in the equivalent time for 690 residual evaluations. The results presented below will show how the method behaves for solving a pseudo steady state problem.

In this report all the unsteady test case have a periodic motion defined by the angle of attack as a function of time given by

$$\alpha(t) = \alpha_m + \alpha_0 \sin(\omega t)$$

where α_m is the mean incidence, α_0 the amplitude of the pitching oscillation and ω the frequency of the pitching motion. All the unsteady calculations are started from the steady flow at the mean incidence. An initial solution at each following time step was obtained by extrapolation from the last two solutions. For these cases the grid is rigidly rotated with the wing.

4 Results

4.1 LANN wing

The LANN wing has a supercritical aerofoil section, leading and trailing edge sweep and high aspect ratio and is typical of a transport type wing. The case considered here has a free stream Mach number of 0.82, $\alpha_m = 0.6^o$, $\alpha_o = 0.25^o$ and $\omega = 0.204$. The wing pitches about an unswept axis at 0.62 of the root chord. Experimental data for this case is given in [17]. Previous calculated inviscid results have been given in [2] and [4]. These show good prediction in the suction peak level but predict the location of the shockwave too far aft. A similar number of grid points in each direction was used for these calculations. In [2] the pseudo time method is used, but the pseudo steady state is solved for by explicit time stepping. In [4] the equations for the updates are similar to equation 3. However, in contrast to the current method these equations are solved by Gauss-Seidel. The number of time steps per cycle used is one hundred, in excess of what is required for time accuracy.

For the current calculations a fine grid was generated which is of C-O topology. This has 249 points in the streamwise direction, 49 points normal to the wing and 49 points around the lower and upper surfaces of the wing. A coarse grid was extracted from this to allow a grid convergence study by removing every second point. The fine grid has roughly 600 thousand points and the coarse grid around 80 thousand. A view of the medium grid around the tip is shown in figure 5. The time for a residual evaluation on the coarse grid on a single pentium 200 processor is 4.56 seconds and for the fine grid on 8 pentium 200 processors connected by a fast ethernet switch is 4.61 seconds.

The results are shown in terms of the pressure distributions at six sections on the wing. The pressure coefficients are analysed to yield mean, in-phase and out-of-phase components. The Fourier analysis is carried out with time $t = 0$ taken from when the wing attains its maximum incidence. These are compared with experiment in figure 1. The fine and coarse grid results using twenty real time steps per cycle are similar except that the first shockwave towards the root is not well resolved on the coarse grid. This can be seen in the plots of the upper surface pressure contours shown in figure 4. The stronger shockwave and the suction peak are well predicted on the medium grid. The comparison with experiment shows that the major discrepancy is in the location of the shockwave, which is predicted too far aft, as for other inviscid calculations.

The comparison of the solutions obtained using twenty and forty real time steps per cycle is shown in figure 2. It is clear that the solution obtained using twenty steps is well converged in time. In fact, the solution obtained using ten real time steps per cycle, which is not shown, is also very accurate.

Finally, the solution obtained using three and four orders reduction in the pseudo steady state residual from the initial value are compared. The converged solution from the previous real time step is used as the starting solution for the pseudo time iterations at the next real time step. The comparison, shown in figure 3 indicates that a three orders reduction is sufficient. The results shown above were obtained using four orders reduction and hence are accurate from this point of view.

A summary of the efficiency of the calculations is given in table 1. The first point to take from this table is that the fine grid calculation is more expensive than the medium grid one at the same conditions. The fine grid solution was obtained on eight Pentium 200 processors whereas the medium grid one was carried out on a single processor. The calculation time increases in proportion with the average number of pseudo time steps needed to calculate the pseudo steady state at each real time step. This indicates that the parallel efficiency of the calculations is almost perfect, a suggestion supported by observing the processor activities during the calculation. The cost of calculating the pseudo steady states is similar to those incurred for two dimensional flows [15], indicating that the method has generalised well to the larger three dimensional problems. The increased cost of the fine grid calculation is possibly due to the better resolution of the weaker shock wave, which is likely to make the pseudo steady state more difficult to calculate [13]. The wall clock times for calculating a cycle are less than 4 hours for the fine grid and 3 hours for the coarse grid.

The tests on the medium grid indicate that the pseudo steady state is more difficult to calculate as the real time step is increased, as expected. The costs of these calcu-

lations using 10,20 and 40 real time steps per cycle are 17.2, 14.5 and 11.4 pseudo steps/real step respectively. This increase however does not offset the computational advantage of doing less real time steps as the real time step is increased. This means that the time step can be chosen to be the largest compatible with time accuracy in the knowledge that using a larger time step will result in a faster calculation. This is not a property shared by all numerical methods where numerical artefacts can lead to efficiency restrictions (see for example [11]).

When using 20 real time steps per cycle it can be seen that there are marginal advantages in using a larger CFL number for the pseudo steady state solution. However, the calculation times only vary by about 25 % between using a CFL of 50 and 200.

In summary, the method yields fast calculation times on a Pentium 200 and the performance of the method is insensitive to the numerical conditions used.

4.2 Results for WEAG-TA15 wing

As a second test case, the flow over the TA15 delta wing pitching to high incidence was calculated. Results where obtained on a C-O grid which consists of $97 \times 33 \times 81$ grid points[1]. The i-direction runs from the apex of the wing to the downstream outer boundary, the j-direction corresponds to the normal direction normal and the k-direction from the symmetry plane in the spanwise direction. The pitch oscillation axis is located at $x/c = 0.5625$ and $z/c = -0.042$ which is in fact below the wing plane. The moment reference point is at $x/c = 0.5625$, $y/c = 0.0$ and $z/c = 0.0$. The Fourier analysis was carried out with time $t = 0$ taken from when the first harmonic attains its maximum.

The experimental data of [20] was measured using a freestream velocity of 40 m/s. The computational results were obtained at a higher Mach number more convenient for a compressible code. A comparison was carried out for the 9^o steady state case to see the effect of increasing the Mach number. The main differences are a slightly higher peak height and less overshoot at the wing edge using $M_\infty = 0.2$. However, the reasonable agreement between the two sets of results justifies using $M_\infty = 0.4$ for the other cases.

Looking at the mean pressure distribution for the 9^o cases shown in figure 6 at an unswept spanwise section running through 80 % root chord, there are two main discrepancies with the experimental data. The first is at the edge of the wing on the upper surface. This is explained by the fact that the Euler equations cannot predict the secondary vortex situated there and also overpredict the primary vortex strength. The other is on the lower surface where the inviscid modelling should be adequate. The difference might be attributed to the wing being mounted on a non negligible belly sting.

[1] the grid was supplied from the collaborative assessment of CFD predictions for this case [5]

Table 3 shows that there is reasonable agreement for the integrated loads in the 9^o case. In the 21^o case, where the vortex, is stronger the agreement is not quite as good. This is due to inviscid modelling being less suited for describing the 21^o case than the 9^o.

A comparison of the first two harmonics of the pressure distribution with experimental data for the $M_\infty = 0.4$ and $\alpha_m = 9.0^o$ case with 40 steps per cycle is shown in figure 6 for the 80% section. The mean value on the upper surface is underpredicted with the vortex too strong and too far towards the wing edge. However the first harmonic is much better predicted on the lower surface, meaning that the unsteady nature of the flow is captured correctly apart from the flow in the vortex itself. The second harmonic shows the correct features which have, however, been shifted towards the wing tip.

A comparison of the pressure distribution with experimental data for the $M_\infty = 0.4$ and $\alpha_m = 21.0^o$ case using 40 steps per cycle is shown in figure 7 for the 80% section. The value of mean pressure on the lower surface is under predicted and the vortex strength over predicted and no secondary vortex is present to stop it moving closer to the wing tip. The first harmonic shows much better agreement with the experimental data on the lower surface. The second harmonic shows the correct features if not the correct values. It is possible to make out the vortex burst at the end of the up cycle near the trailing edge of the wing. Figure 8 showns the pressure-loss though the vortex at 80% chord. It can be seen that the vortex separates from the wing in the downstoke as well as becoming weaker. By the time $\alpha = 21^o$ on the upstroke the vortex had reattached and is growing in size.

The calculation at a mean incidence of 21^o requires around 12 hours per cycle using 40 real time steps per cycle on 4 Pentium 200 processors.

4.3 Results for F5 wing

The final set of results if for the F5 wing undergoing small amplitude pitching. Calculations were carried out over a range of Mach numbers for the clean wing. The cases are summarised in table 4 with the pitching being about an unswept axis through half root chord. The F5 wing is typical of a fighter wing, with small aspect ratio, high leading edge sweep and is around 5 % thick. Experimental data for all the cases is available in [10] [9]. Previous calculated results have been shown in [4] for case 160, where the calculation details were as for the LANN calculations described above, i.e. 100 real time steps per cycle was used.

For these calculations a C-O grid with 125 points in the streamwise direction, 25 points normal and 25 points in the spanwise direction was used. The time for a residual evaluation on this grid is 4.56 seconds on a single Pentium 200 processor. Calculations for the clean wing cases were carried out using 20 steps per cycle and the pseudo tolerance was four orders. The comparison with exper-

iment for the Fourier decomposed pressure distributions is shown in figures 9 - 14. The agreement with experiment is generally good with problems encountered in the levels and locations of the peaks in the real and imaginary parts, due to the absence of viscous effects from the calculations.

The pressure contours on the upper surface for case 160 are shown in figure 15. The major flow feature is the shockwave located towards the trailing edge.

The performance of the calculations is summarised in table 5. The results are similar to those obtained for the LANN wing. The calculations seem to take longer for the Mach numbers about 1.0, suggesting that the shock motions are more significant at these conditions. The behaviour of the case 172 with time step is again very similar to that observed for the LANN wing i.e. the number of pseudo steps required at each real time step increases with real time step, but the overall cost of the calculation is reduced to to the lower number of real time steps required.

5 Conclusions

The speed of the current method has been demonstrated. Three dimensional unsteady calculations have been performed on a small number of Penitium 200 processors in the order of hours. This level of performance makes it realistic to start considering unsteady viscous calculations. Preliminary laminar cavity calculations have yielded encouraging results.

The main conclusions from this work are that for these test cases

- the real time step can be chosen for time accuracy alone
- the cost of these calculations is very similar in terms of pseudo time iterations to 2d calculations
- the cost does not increase significantly with the real time step.

Future work involves the extension of the method for viscous flows and its application to problems with deforming geometries.

Acknowledgements

This work was partially supported BAe contract (SP050104458), Defence and Evaluation Research Agency (DERA) contract FRNI c/107 and EPSRC (GR/K55455).

References

[1] A.Jameson, 'Time dependent calculations using multigrid, with applications to unsteady flows past airfoils and wings', Technical report, AIAA 91-1596, (1991).

[2] A.L.Gaitonde, 'A dual-time method for the solution of the unsteady Euler equations', *Aeronautical Journal*, **10**, 283–291, (1994).

[3] B.J.Gribben, K.J.Badcock, and B.E.Richards, 'Application of PMB2D to axisymmetric flows', Aerospace Engineering Report, 12, Glasgow University, Glasgow, UK, (1998).

[4] A. Brenneis and A. Eberle, 'Application of an implicit relaxation method solving the Euler equations for time-accurate unsteady problems', *Journal of Fluids Engineering*, **112**, 510–520, (1990).

[5] N. Cerosola, 'Weag ta15 common exercise iv time accurate calculations of vortical flow on a delta wing in pitching motion. final report', Technical report, Alenia report number 65/RT/T302/98182 issue 1 24/8/98, (1998).

[6] A.D'Alascio et al, 'First results of the EROS european unsteady Euler code on overlapping grids', in *Fourth European conference on CFD*, pp. 694–703. ECCOMAS, (1998).

[7] F.Cantariti, L.Dubuc, B.Gribben, M.Woodgate, K.J.Badcock, and B.E.Richards, 'Approximate Jacobians for the solution of the Euler and Navier-Stokes equations', Aerospace Engineering Report, 5, Glasgow University, Glasgow, UK, (1997).

[8] G.P. Guruswamy, 'Unsteady aerodynamic and aeroelastic calculations for wings using Euler equations', *AIAA Journal*, **28**, 461–469, (1990).

[9] J.W.G Van Nunen et al H.Tidjeman, 'Transonic wind tunnel tests of an oscillating wing with external store (parts i-iv)', Technical Report 78106, NLR, (1978).

[10] H.Tidjeman et al J.W.G Van Nunen, 'Results of transonic wind tunnel meaurements on an oscillating wing with external store (data report)', Technical Report 78030, NLR, (1978).

[11] K.J.Badcock and A.L.Gaitonde, 'An unfactored method with moving meshes for solution of the Navier-Stokes equations for flows about aerofoils', *International Journal of Numerical Methods in Fluids*, **23**, 607, (1996).

[12] K.J.Badcock and B.E.Richards, 'Implicit time stepping methods for the Navier-Stokes equations', *AIAA Journal*, **34**, 555, (1996).

[13] K.J.Badcock, F.Cantariti, I.Hawkins, B.Gribben, L.Dubuc, and B.E.Richards, 'Simulation of unsteady turbulent flows using the pseudo time method', Aerospace Engineering Report,submitted for

publication 21, Glasgow University, Glasgow, UK, (1997).

[14] K.J.Badcock, S.Porter, and B.E.Richards, 'Unfactored multiblock methods:Part I initial method development', Aerospace Engineering Report 11, Glasgow University, Glasgow, UK, (1995).

[15] L.Dubuc, F.Cantariti, M.Woodgate, B.Gribben, K.J.Badcock, and B.E.Richards, 'A grid deformation technique for unsteady flow computations', Aerospace Engineering Report,submitted for publication 21, Glasgow University, Glasgow, UK, (1998).

[16] F. Cantariti M. Woodgate, K. Badcock and B. Richards, 'Solution of the Euler equations in three dimensions using a fully unfactored method', Aerospace Engineering Report 8, Glasgow University, Glasgow, UK, (1999).

[17] R.J.Zwaan, 'LANN wing , pitching oscillation in compendium of unsteady aerodynamic measurements addendum 1', Technical Report 702, AGARD, (1985).

[18] L.B. Simpson and D.L. Whitfield, 'Flux-difference split algorithm for unsteady thin-layer Navier-Stokes solutions', *AIAA Journal*, **30**, 914–922, (1992).

[19] S.Osher and S.R.Chakravarthy, 'Upwind schemes and boundary conditions with applications to Euler equations in general coordinates', *Journal Computational Physics*, **50**, 447–481, (1983).

[20] T.Loser, 'Dynamic force and pressure measurements on an oscillating delta wing at low speeds', Technical report, DLR report 1 B 129-96/9, (1996).

Grid	Processors	Real time steps per cycle	CFL	Average number of pseudo time steps per real time step	CPU time (in Work Units)
Fine	8	20	100	20.9	2668
Medium	1	20	100	14.5	1668
Medium	1	10	100	17.2	1017
Medium	1	40	100	11.4	2490
Medium	1	20	200	13.0	1538
Medium	1	20	50	17.2	1903

Table 1: Summary of performance for different calculation details for LANN wing test case.

Table 2: WEAG-TA15 wing test cases

M_∞	α_m	α_0	ω	steps cycle
0.2	9.0			
0.4	9.0			
0.4	21.0			
0.4	9.0	6.0	0.56	40
0.4	9.0	6.0	0.56	40
0.4	21.0	6.0	0.56	80

Table 3: Integrated loads for WEAG-TA15 wing test cases

M_∞	α_m	C_L	C_D	C_m
Exp	9.0	0.37	0.05	-0.0001
Exp	21.0	0.79	0.33	0.0005
0.2	9.0	0.4151	0.05647	-0.00700
0.4	9.0	0.4201	0.05719	-0.00936
0.4	21.0	1.0548	0.38090	-0.00559

Table 4: F5 wing test cases

Case	M_∞	α_m	α_0	ω
383	0.597	0.004	0.115	0.798
370	0.896	0.001	0.275	0.550
160	0.947	-0.006	0.132	0.264
373	1.092	0.003	0.058	0.116
172	1.093	0.003	0.116	0.232
193	1.336	-0.001	0.198	0.396

Case	Processors	Real time steps per cycle	CFL	Average number of pseudo time steps per real time step	CPU time (in Work Units)
383	1	20	100	8.8	1869
370	1	20	100	14.2	2713
160	1	20	100	19.6	3681
373	1	20	100	12.4	2628
172	1	20	100	14.4	2813
172	1	10	100	15.8	1677
172	1	40	100	11.3	4338
193	1	20	100	9.1	1527

Table 5: Summary of performance for F5 wing test cases.

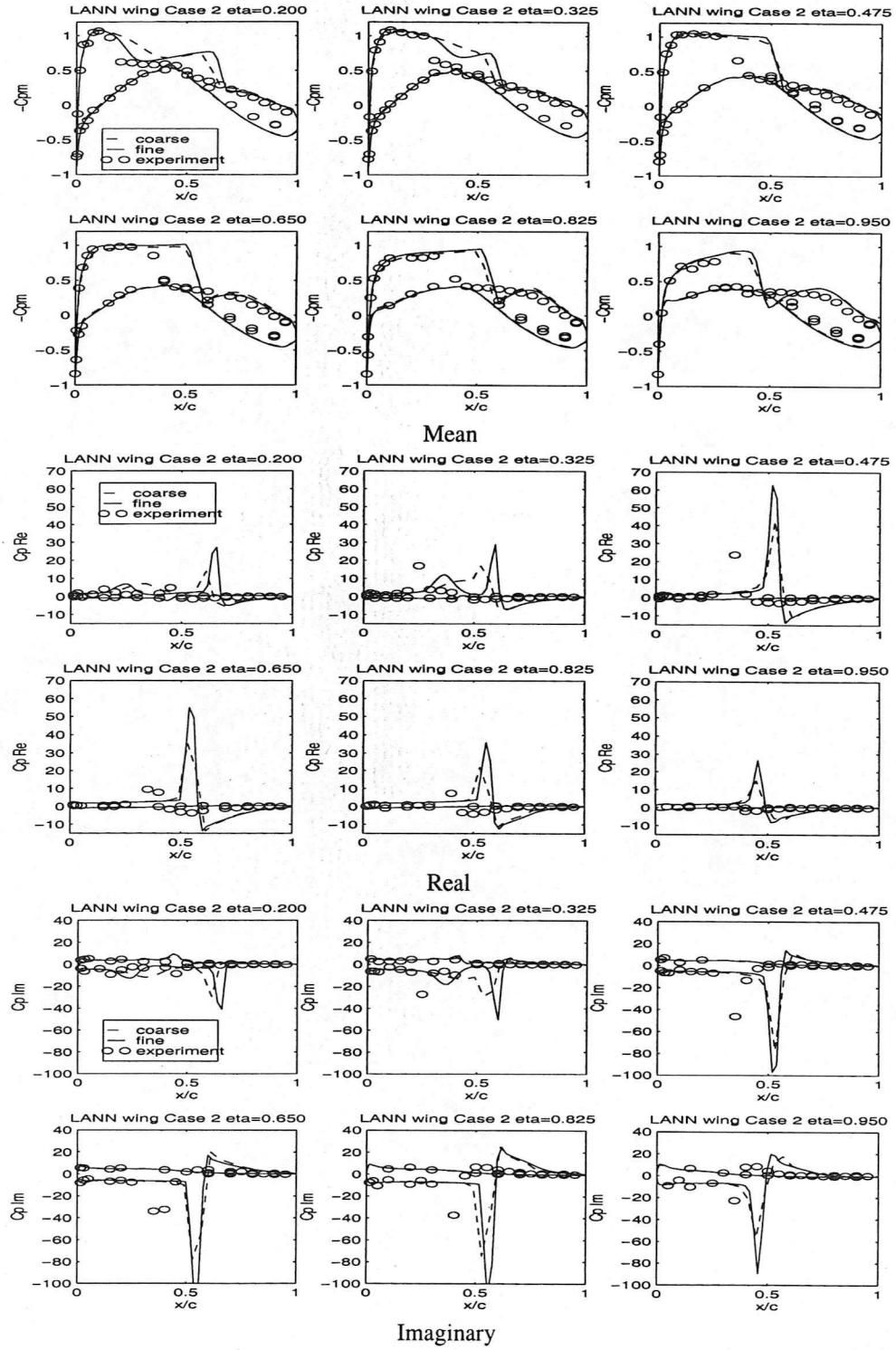

Figure 1: **Comparison between coarse and fine grid solutions and experimental data for mean, real and imaginary pressure coefficients**

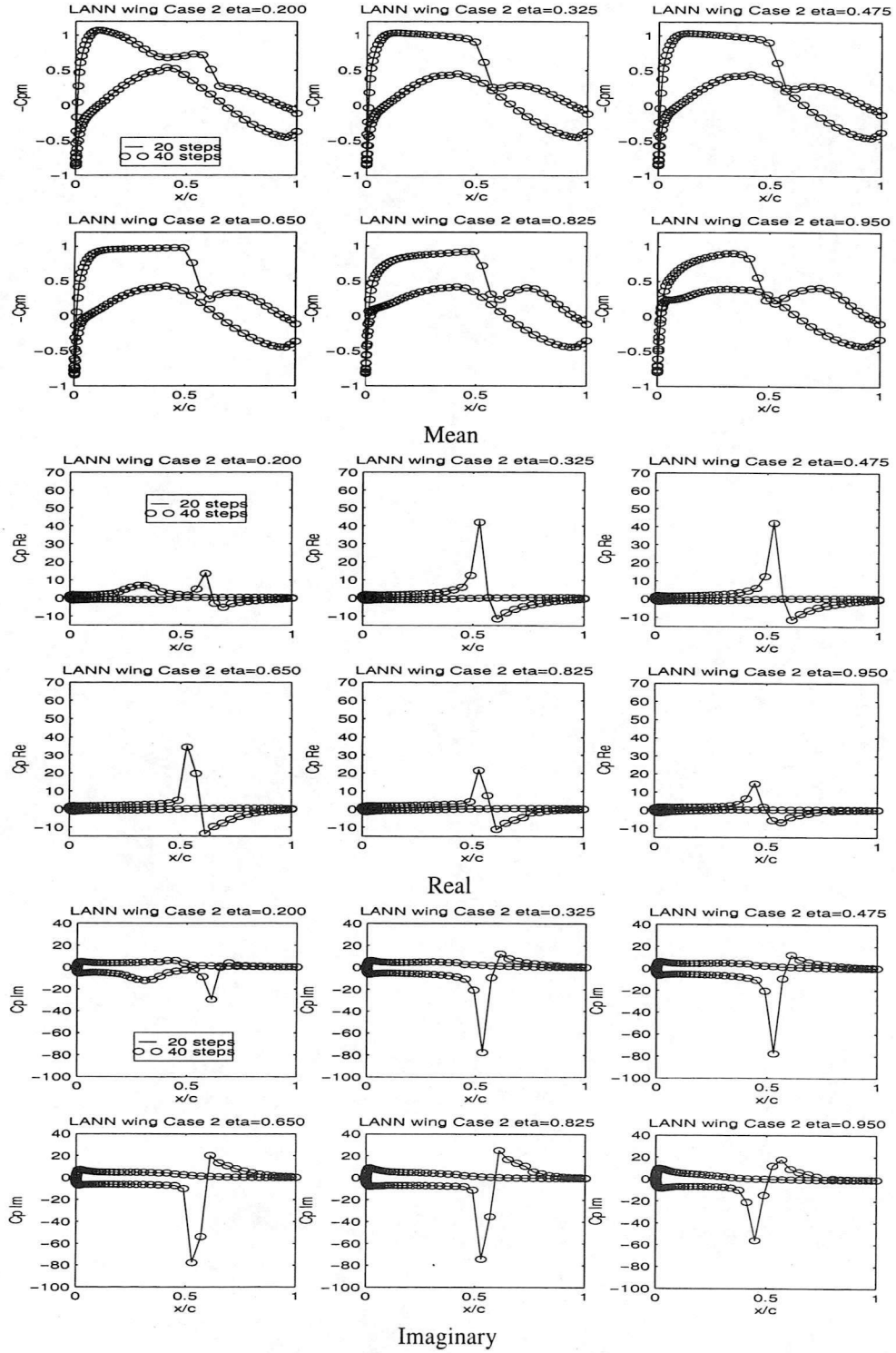

Figure 2: **LANN test case: comparison between solutions using 20 and 40 steps per cycle.**

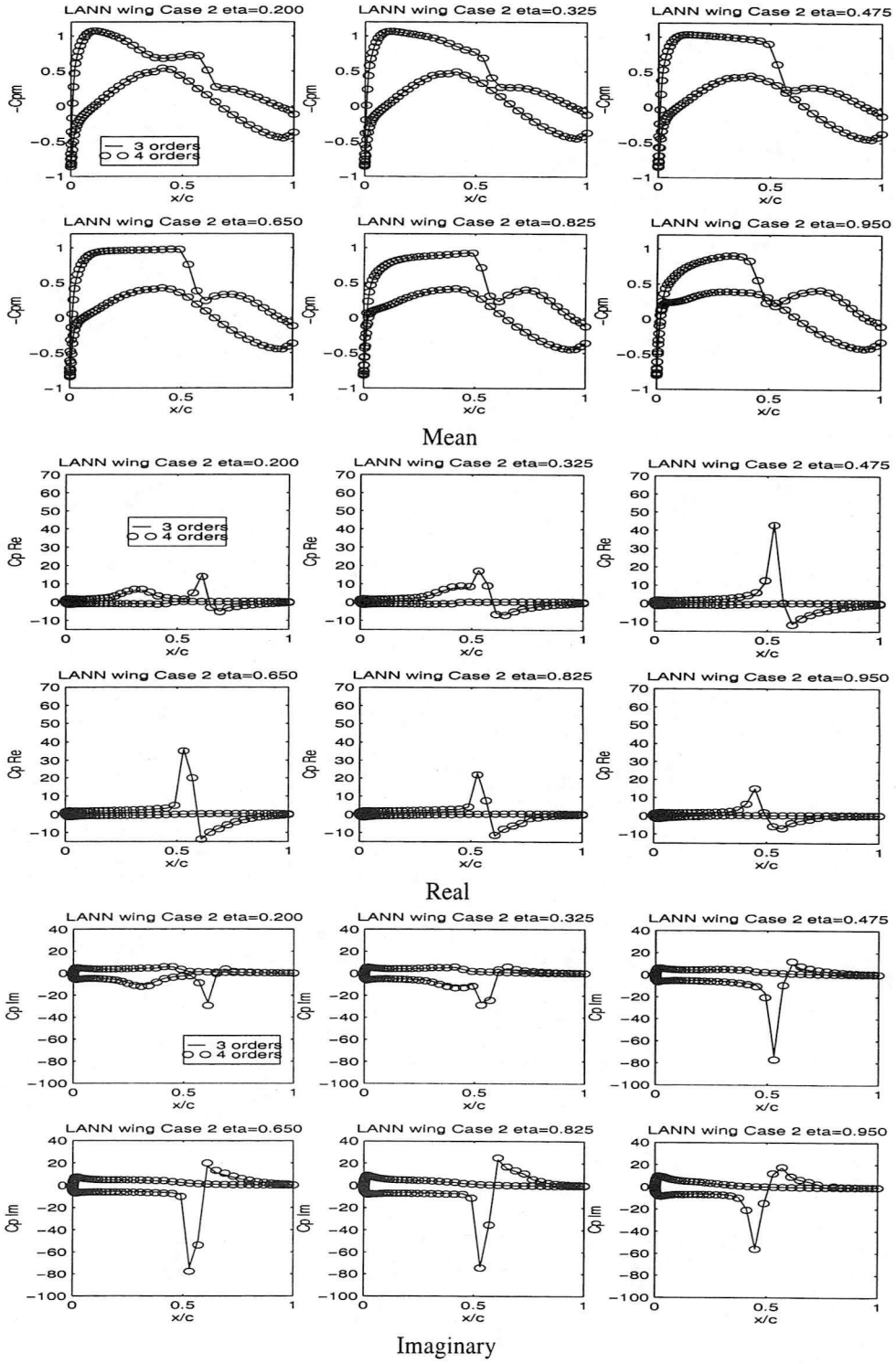

Figure 3: **LANN test case: comparison between solutions using using 3 and 4 orders reduction in the pseudo residual at each real time step.**

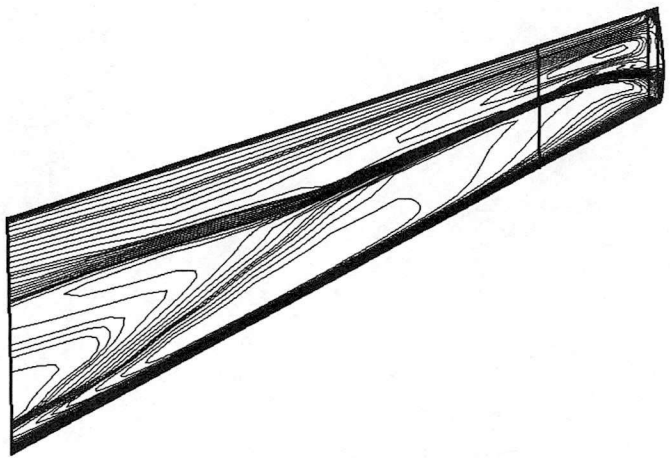

medium grid

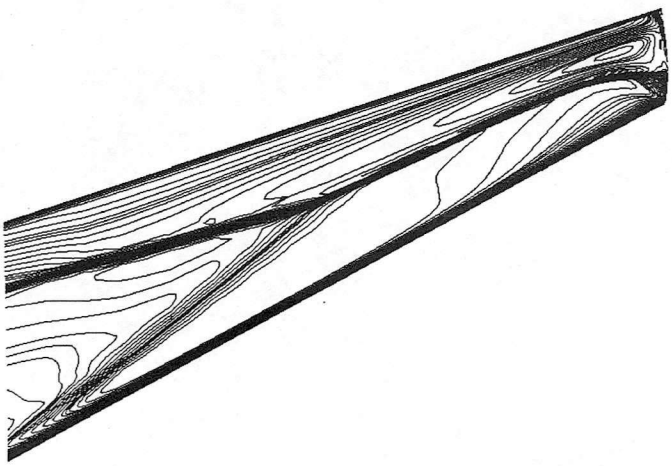

fine grid

Figure 4: **LANN test case: pressure contours on upper surface for converged steady state solution at mean incidence.**

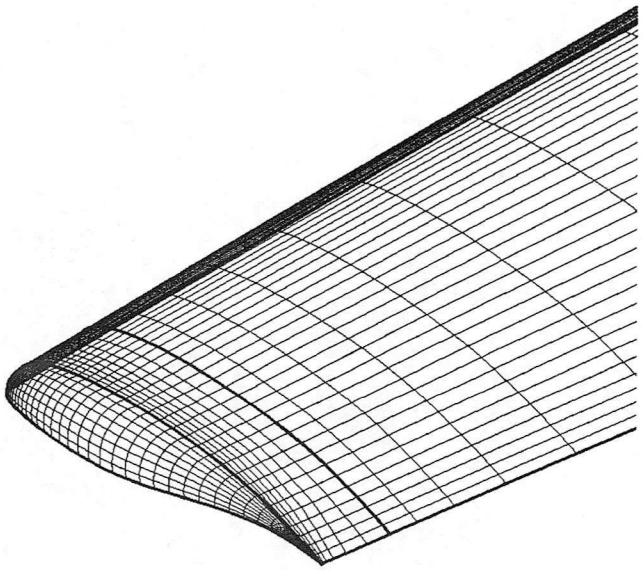

medium grid

Figure 5: **LANN test case: grid in the region of the wing tip.**

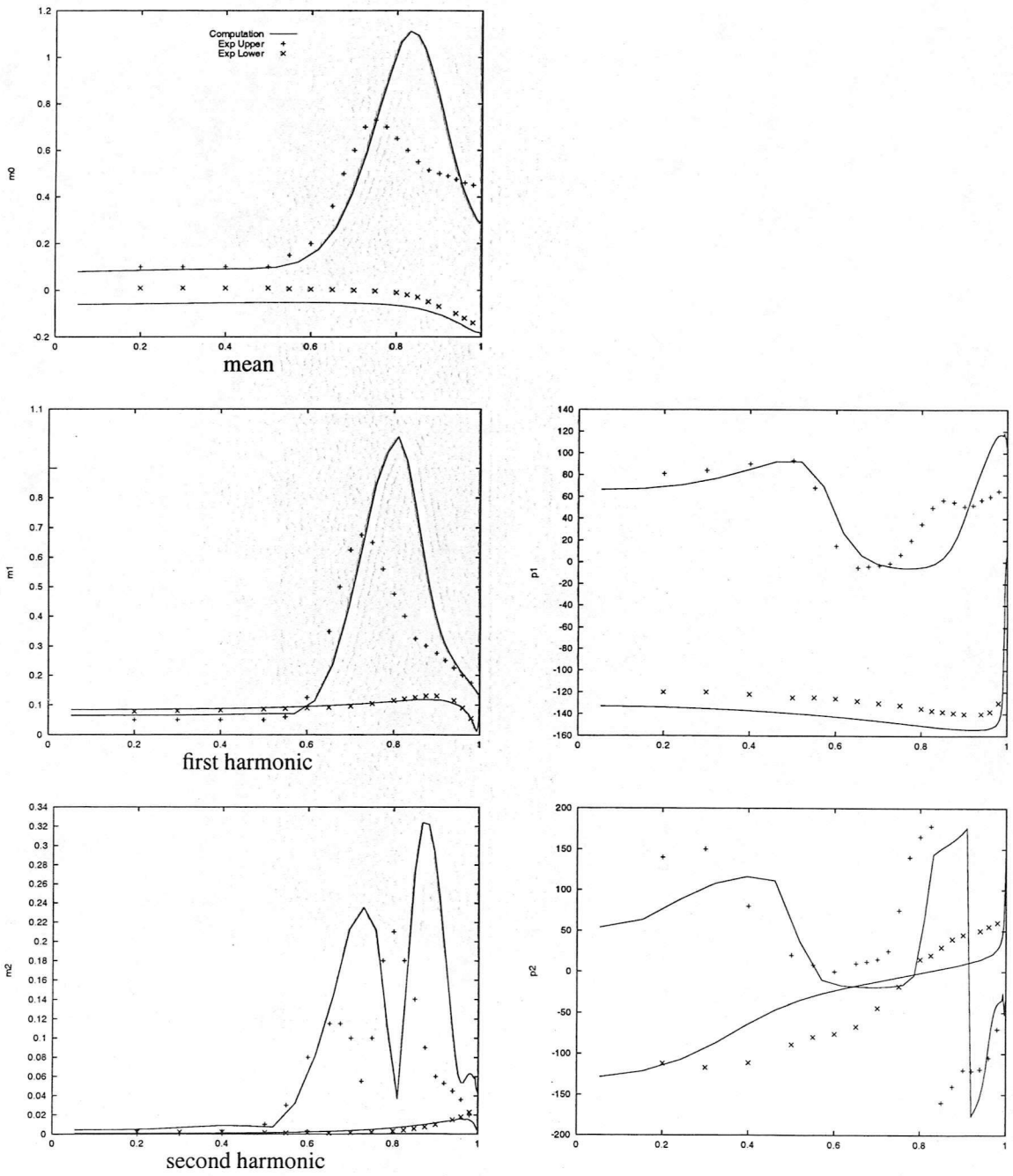

Figure 6: **Delta wing test case: pressure coefficient at 0.8 % chord for the unsteady state case at 9^o mean incidence.**

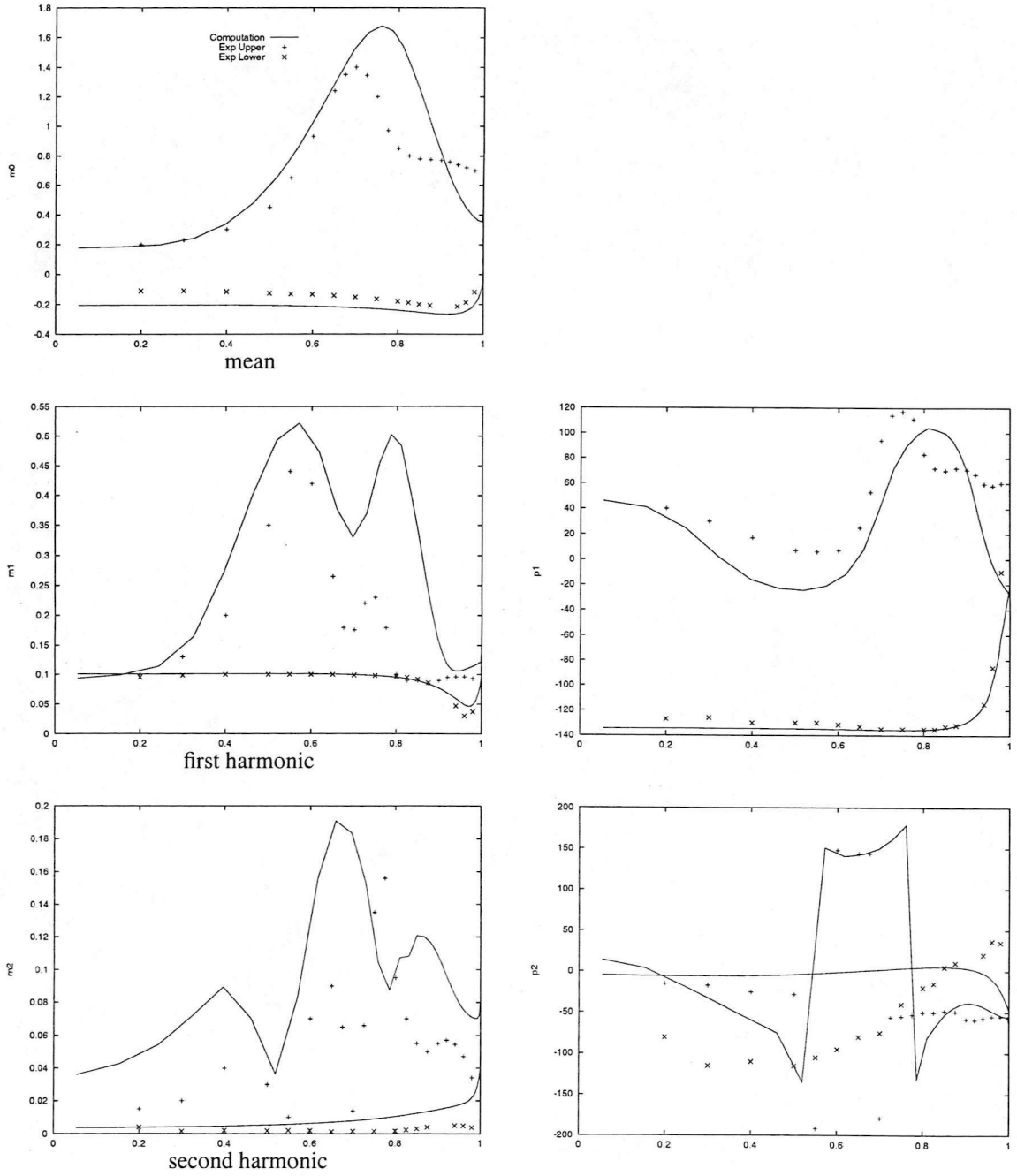

Figure 7: **Delta wing test case: pressure coefficient at 0.8 % chord for the unsteady state case at** 21^o **mean incidence.**

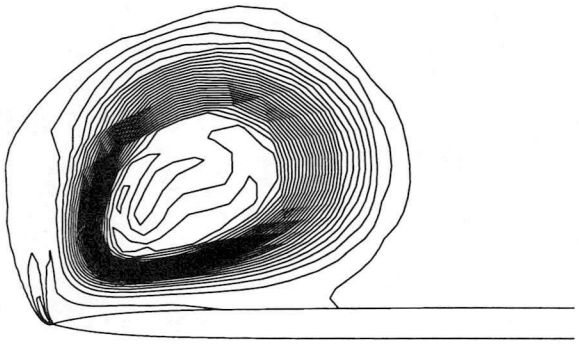

27^o

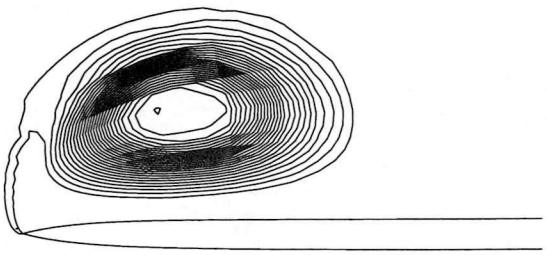

21^o

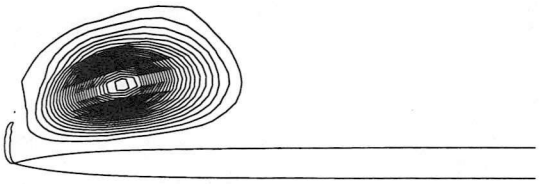

15^o

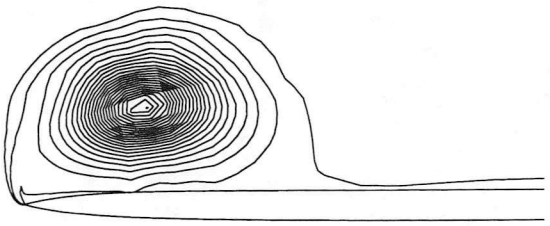

21^o

Figure 8: **Delta wing test case: pressure loss contours at 0.8 % chord for the unsteady state case at 21^o mean incidence.**

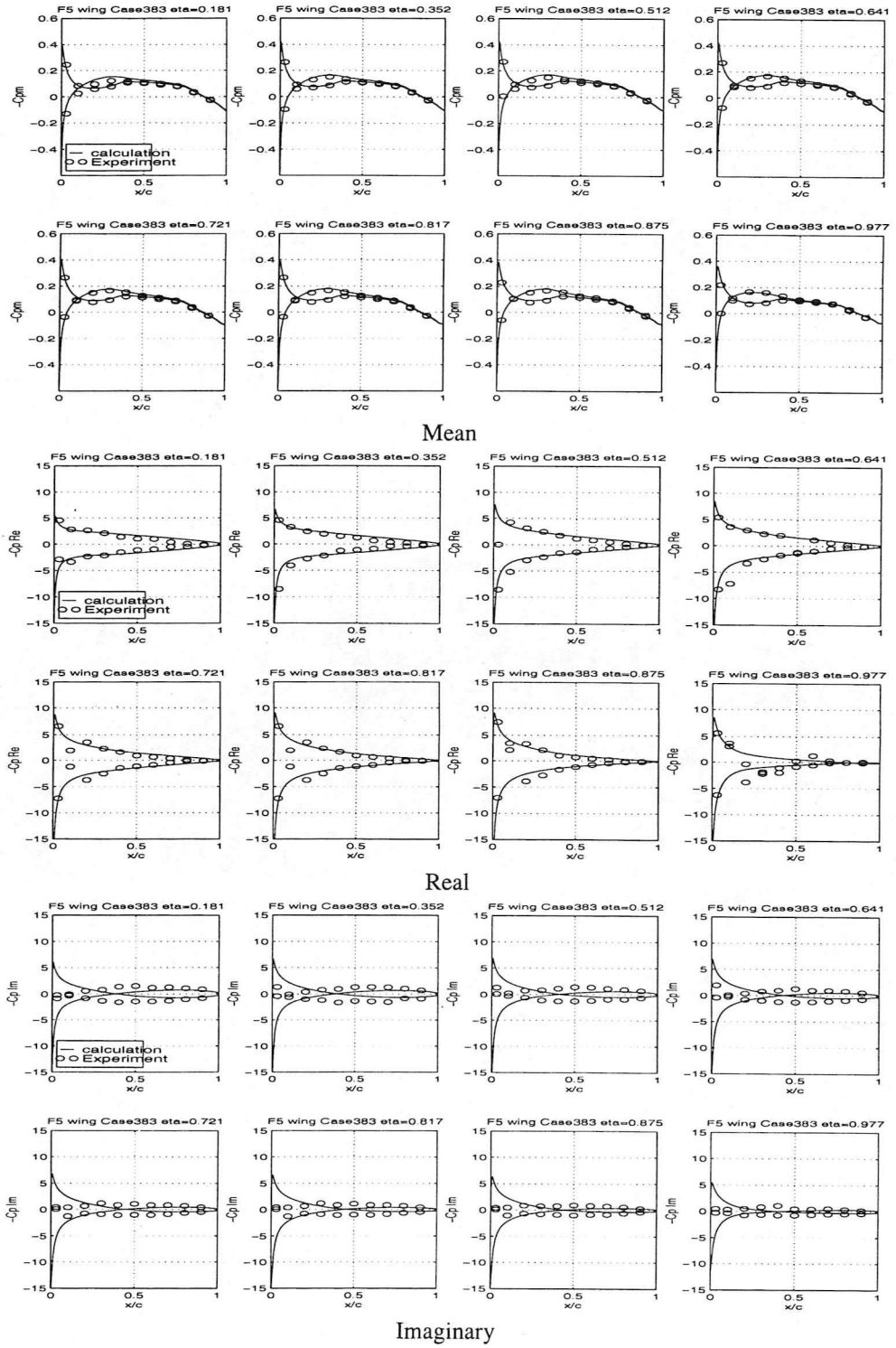

Figure 9: **Comparison between computed and experimental data for mean, real and imaginary pressure coefficients for F5 wing case 383**

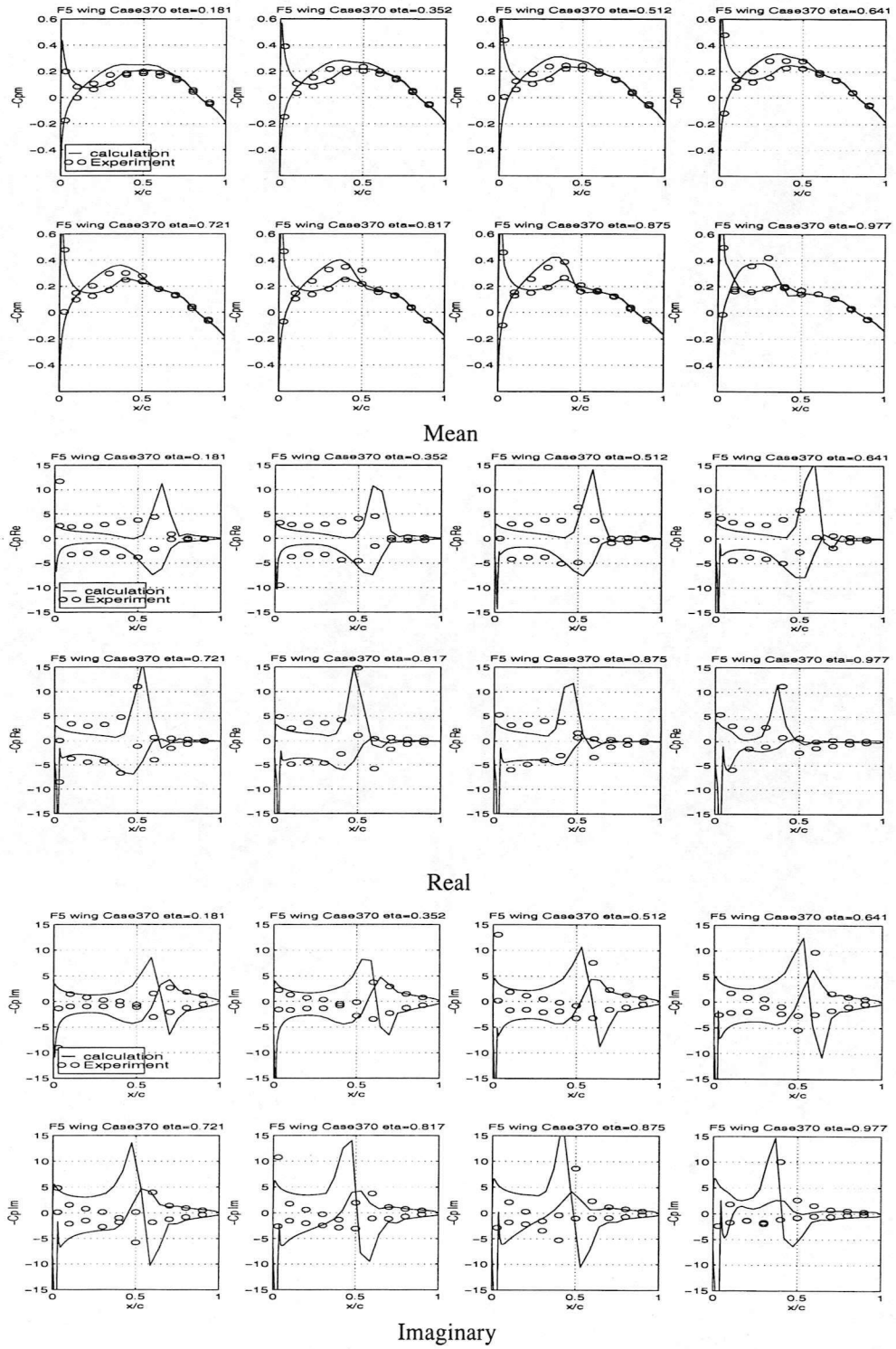

Figure 10: **Comparison between computed and experimental data for mean, real and imaginary pressure coefficients for F5 wing case 370**

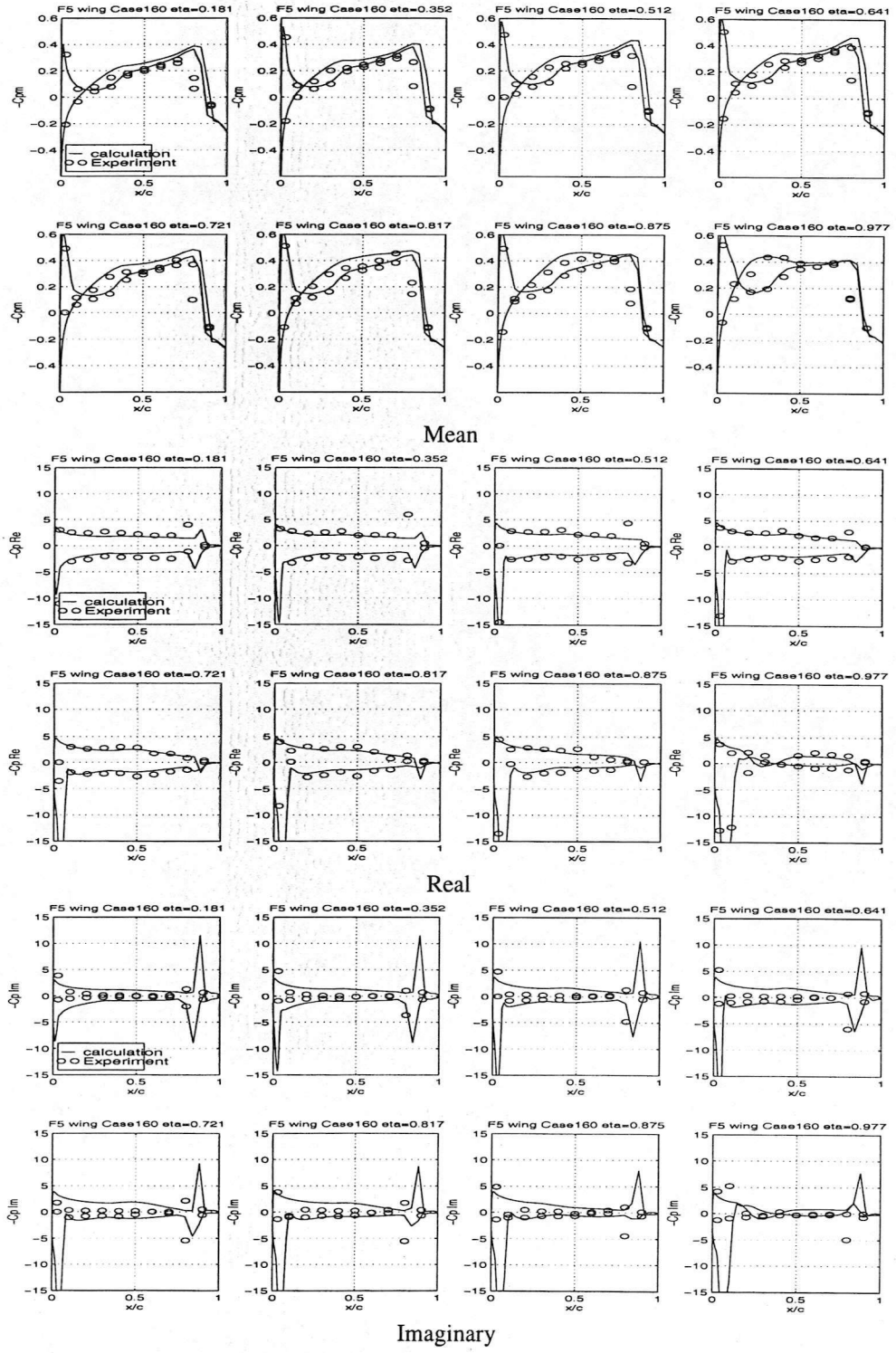

Figure 11: **Comparison between computed and experimental data for mean, real and imaginary pressure coefficients for F5 wing case 160**

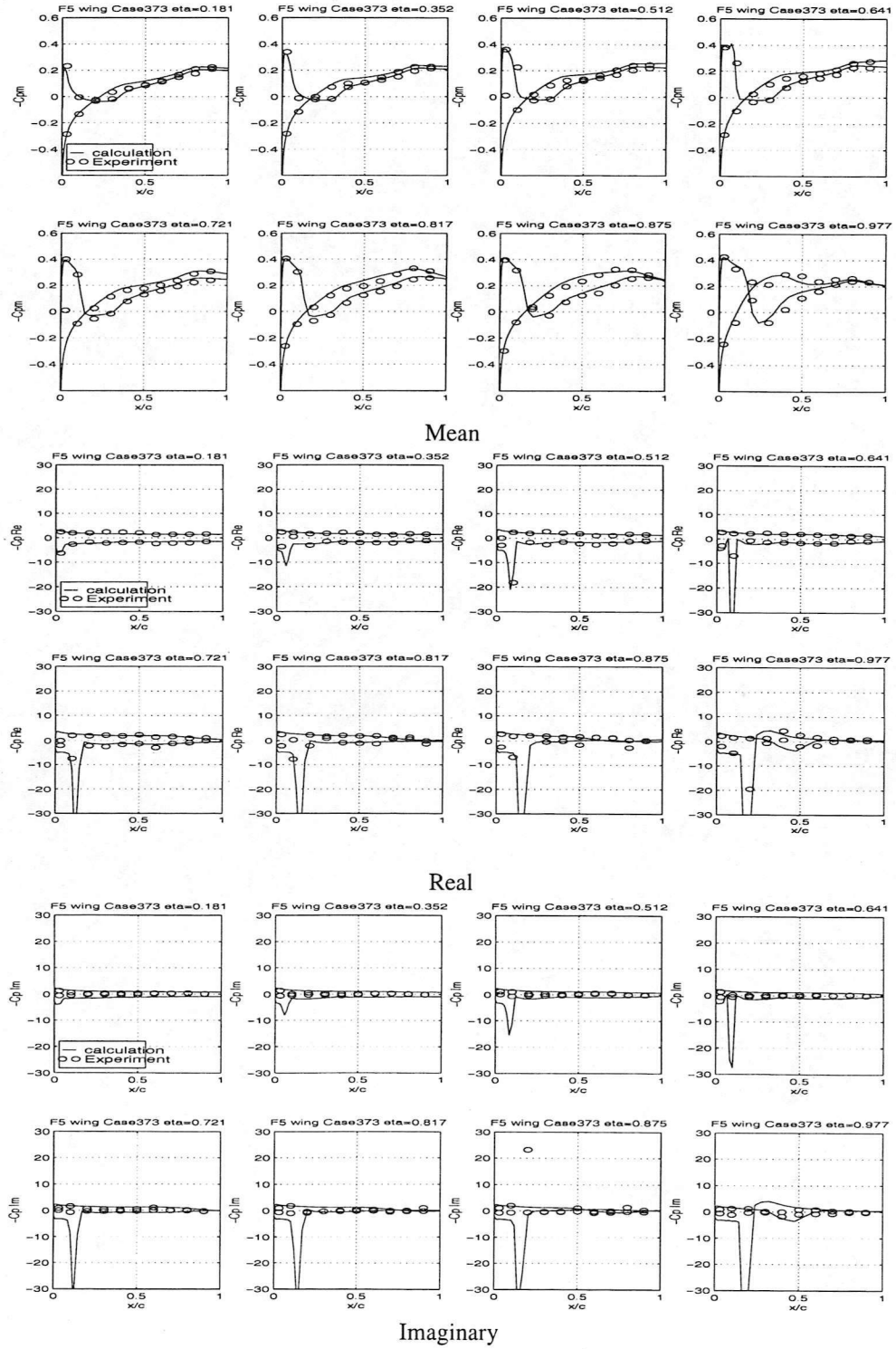

Figure 12: **Comparison between computed and experimental data for mean, real and imaginary pressure coefficients for F5 wing case 373**

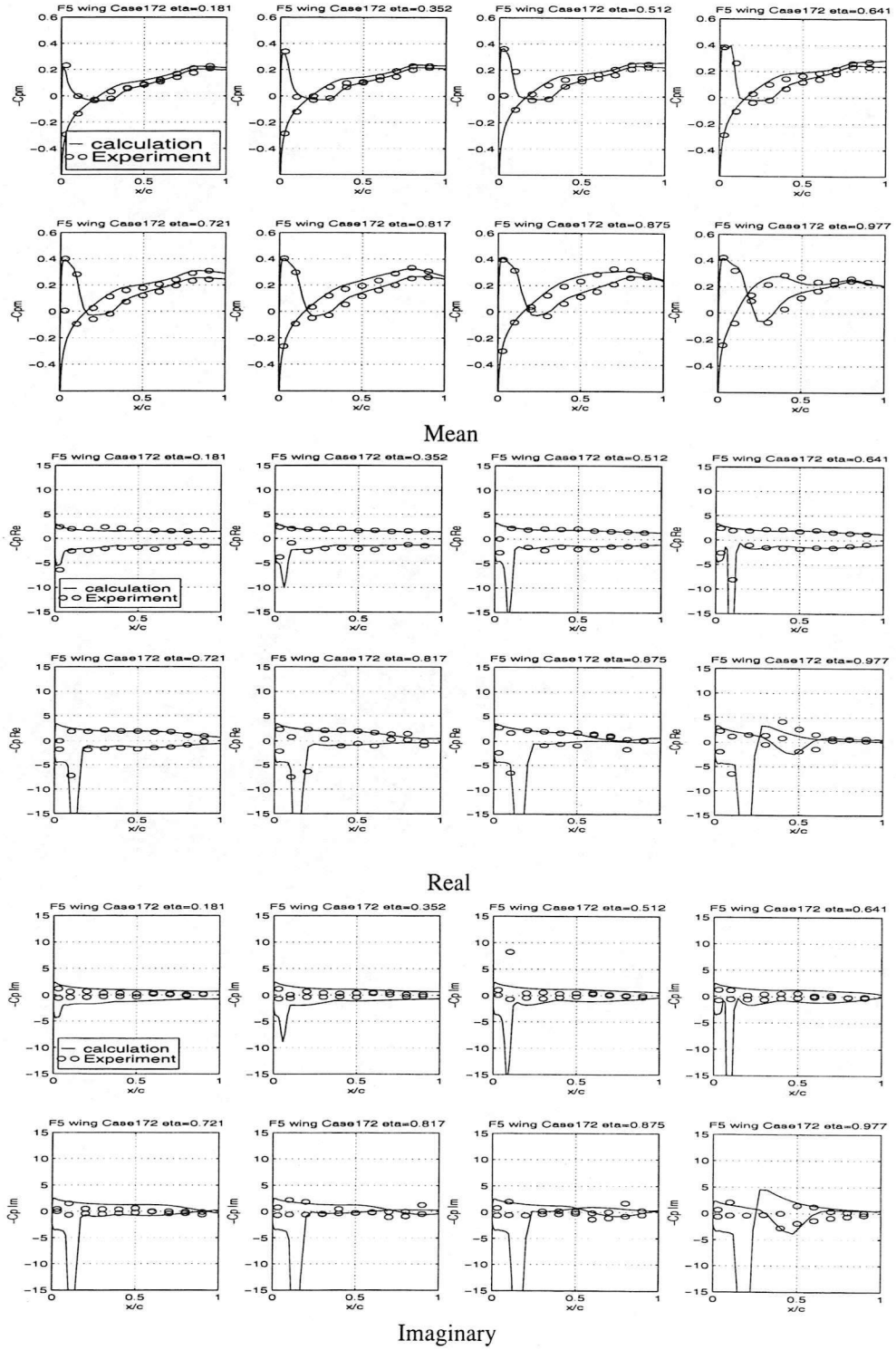

Figure 13: **Comparison between computed and experimental data for mean, real and imaginary pressure coefficients for F5 wing case 172**

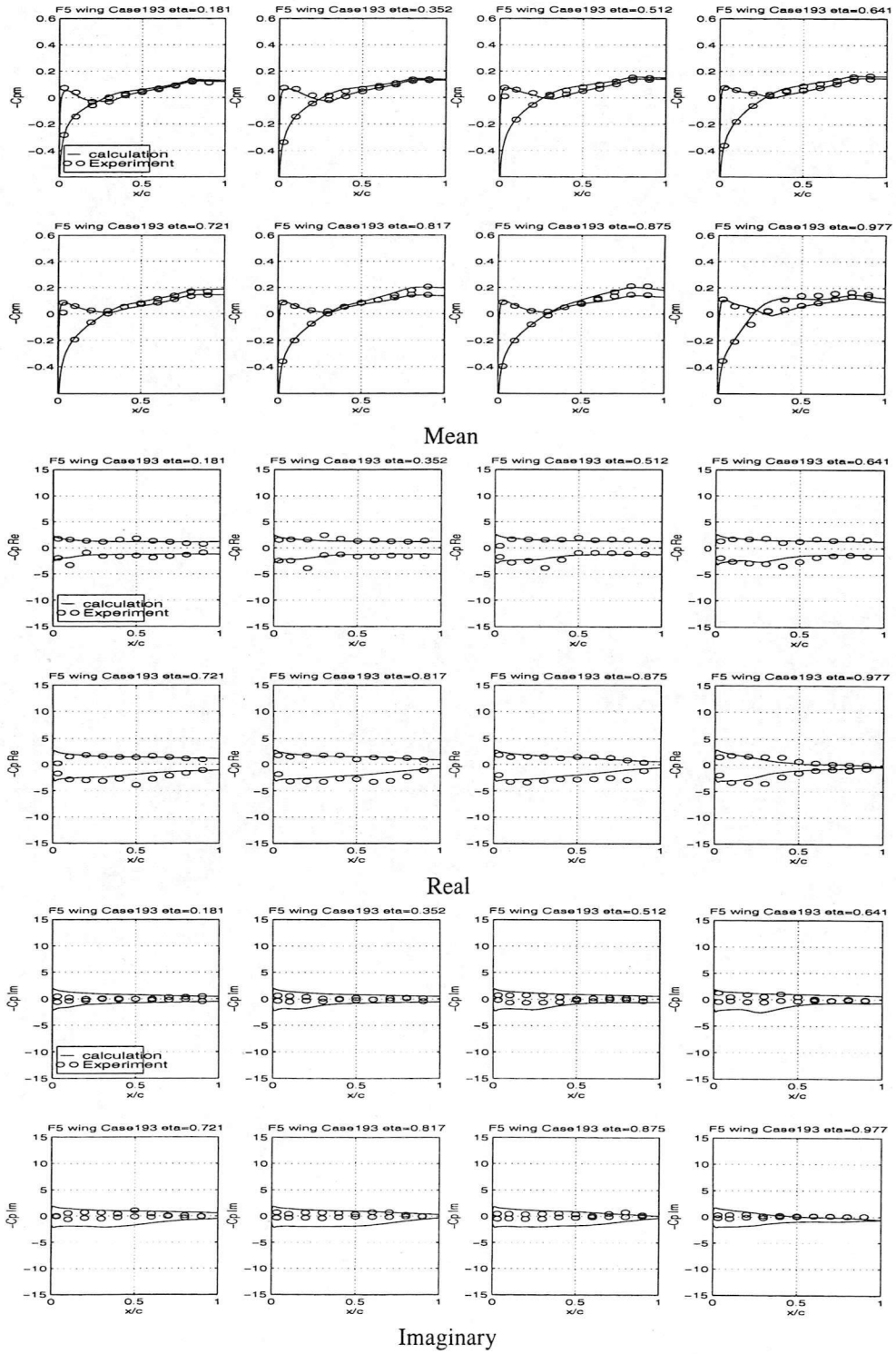

Figure 14: **Comparison between computed and experimental data for mean, real and imaginary pressure coefficients for F5 wing case 193**

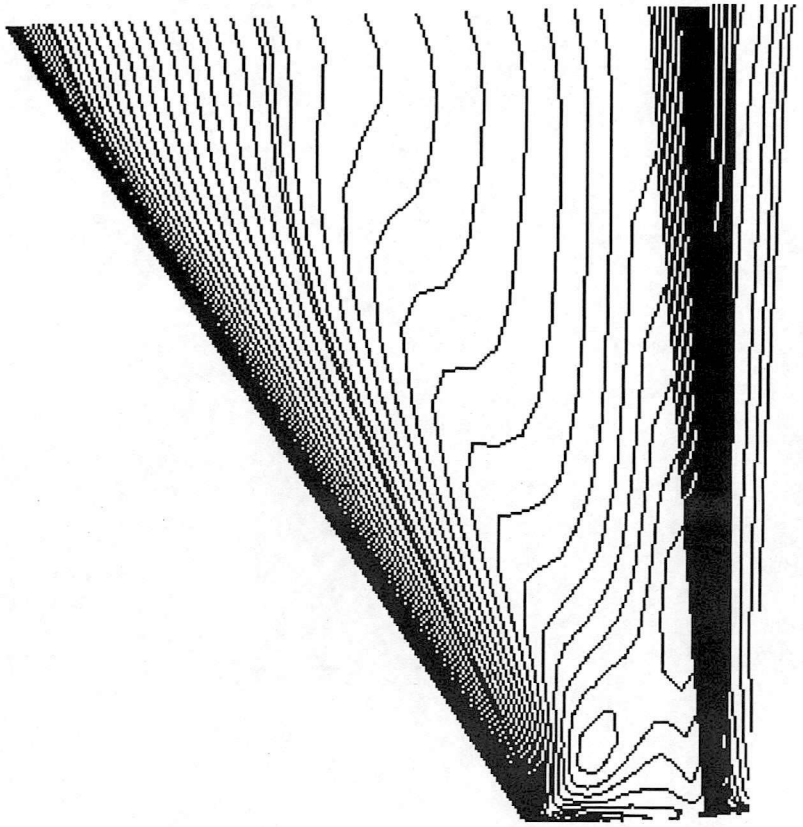

Figure 15: **F5 test case 160: pressure contours on upper surface for converged steady state solution at mean incidence.**